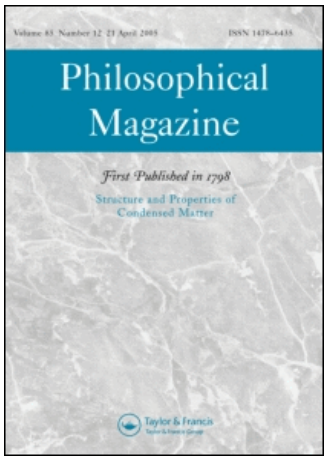

Philosophical Magazine
First published in 1798
Publication details, including instructions for authors and subscription information:
http://www.informaworld.com/smpp/title~content=t713695589

Disorder trapping and grain refinement during solidification of undercooled Fe-18 at% Ge melts

First Published on: 08 June 2007
To cite this Article: Biswas, K., Phanikumar, G., Holland-Moritz, D., Herlach, Dieter M. and Chattopadhyay, K. , 'Disorder trapping and grain refinement during solidification of undercooled Fe-18 at% Ge melts', Philosophical Magazine, 1 - 21
To link to this article: DOI: 10.1080/14786430701420549
URL: http://dx.doi.org/10.1080/14786430701420549

Philosophical Magazine,
2007, 1–21, iFirst

Disorder trapping and grain refinement during solidification of undercooled Fe–18 at% Ge melts

K. BISWAS*†¶, G. PHANIKUMAR‡,
D. HOLLAND-MORITZ§, DIETER M. HERLACH§ and
K. CHATTOPADHYAY†

†Department of Materials Engineering, Indian Institute of Science,
Bangalore 560012, India
‡Department of Metallurgical and Materials Engineering,
Indian Institute of Technology Madras, Chennai 600036, India
§Institute of Space Simulation, German Aerospace Centre (DLR),
Linder Höhe, 51147 Köln, Germany

(*Received 28 January 2007; in final form 9 April 2007*)

The electromagnetic levitation technique has been used to systematically study microstructure evolution and growth rate as a function of undercooling in concentrated Fe–18 at% Ge alloy. The samples are undercooled to a maximum of 240 K. Growth-rate analysis and transmission electron microscopy reveal that, beyond an undercooling of 120 K, the primary phase to solidify is disordered. Microstructural investigations show a decrease in grain size with increasing undercooling. Orientation-imaging microscopy using electron back-scattered diffraction (EBSD) and microhardness measurements have been used to show that recovery and recrystallization play a significant role in the evolution of final microstructure. Microstructural evolution has also been discussed in light of current models of dendrite growth and grain refinement.

1. Introduction

The emergence of phases during solidification is controlled by the kinetics of nucleation and growth. One of the important parameters controlling the kinetics of both these processes is the melt undercooling [1, 2]. In the case of container-less processing [1], undercooling can be a control parameter, chosen by triggering the crystallization at a desired temperature or level of undercooling. Thus, it is possible to study development of microstructure and phase evolution as a function of undercooling.

Rapid solidification behaviour of ordered intermetallics has been extensively studied both experimentally and theoretically. High growth rates of primary phase can reduce the chemical order in the intermetallic compounds [2] and even disordered phases can form directly from the melt [3]. Such solids can order when atoms diffuse

*Corresponding author. Email: krisbis1@gmail.com
¶Present address: Institute for Multidisplinary Research on Advanced Materials, Tohoku University, Sendai 980-8577, Japan.

Philosophical Magazine
ISSN 1478–6435 print/ISSN 1478–6443 online © 2007 Taylor & Francis
http://www.tandf.co.uk/journals
DOI: 10.1080/14786430701420549

into different sub-lattices during subsequent solid-state cooling to room temperature, resulting in the formation of fine anti-phase domains. This is known as disorder trapping, which is akin to solute trapping in case of disordered solid solutions. A reliable method of proving experimentally that an intermetallic solidified initially in a disordered form is the microstructural observation of a high density of anti-phase domains.

An intrinsic grain-refinement effect in undercooled melt has also been studied [4, 5]. Essentially, the effect is an abrupt change at a well-defined undercooling from coarse columnar to a fine equiaxial grain structure. Several theories have been proposed to explain the spontaneous grain refinement during solidification of the undercooled melts, such as dynamic nucleation, remelting and recovery and recrystallization. Therefore, a detailed study is necessary to identify a possible mechanism for the system under study.

The aim of the present investigation is to understand the nucleation and growth behaviour of iron-rich Fe–18 at% Ge alloy with special emphasis on disorder trapping and grain refinement during the process of undercooling and subsequent solidification.

The Fe-rich portion of the Fe–Ge phase diagram [6] is shown in figure 1. It shows presence of a number of critical points and order–disorder transformations [7]. The composition studied in the present investigation is marked on the diagram. The present alloy composition lies in the boundary of the B2 ordering transition line intersecting the liquidus. According to the phase diagram, the solidification of this alloy will start with nucleation of the bcc phase (α-FeGe solid solution, $a = 0.288$ nm). However, B2 phase may form under non-equilibrium solidification conditions due to dendrite coring. Coring is a form of non-equilibrium micro-segregation, which is caused by cellular/dendrite freezing of alloys. The primary dendrite arms, which shoot into the undercooled melt, contains less solute than the interdendritic regions. These interdendritic regions become enriched in solutes and, thus, become the regions high in solute concentrations. At lower temperatures ($<700^{\circ}$C), B2 phase undergoes solid-state transformation to α_1 (DO_3, $a = 0.576$ nm) phase.

2. Experiments

Samples of nominal composition Fe–18 at% Ge were prepared by arc melting pure components with purity >99.99%. The samples were repeatedly melted on a water-cooled copper hearth to obtain a homogeneous composition. The undercooling experiments were carried out using an electromagnetic levitation facility [8]. Sample of $\sim$1 g in weight and 6–7 mm in diameter was inserted into the levitation coil inside the vacuum chamber and held using an alumina tube. The chamber was evacuated to a level of 10^{-6} mbar and subsequently refilled with a reducing protective gas (He+5 vol% H_2) of 99.9999% purity to 1000 mbar pressure. After the sample was levitated, the sample holder was withdrawn. Simultaneously, the sample was heated by induction to a temperature above the liquidus and held for few minutes for homogenization. It was then undercooled by blowing the protective gas mixture on

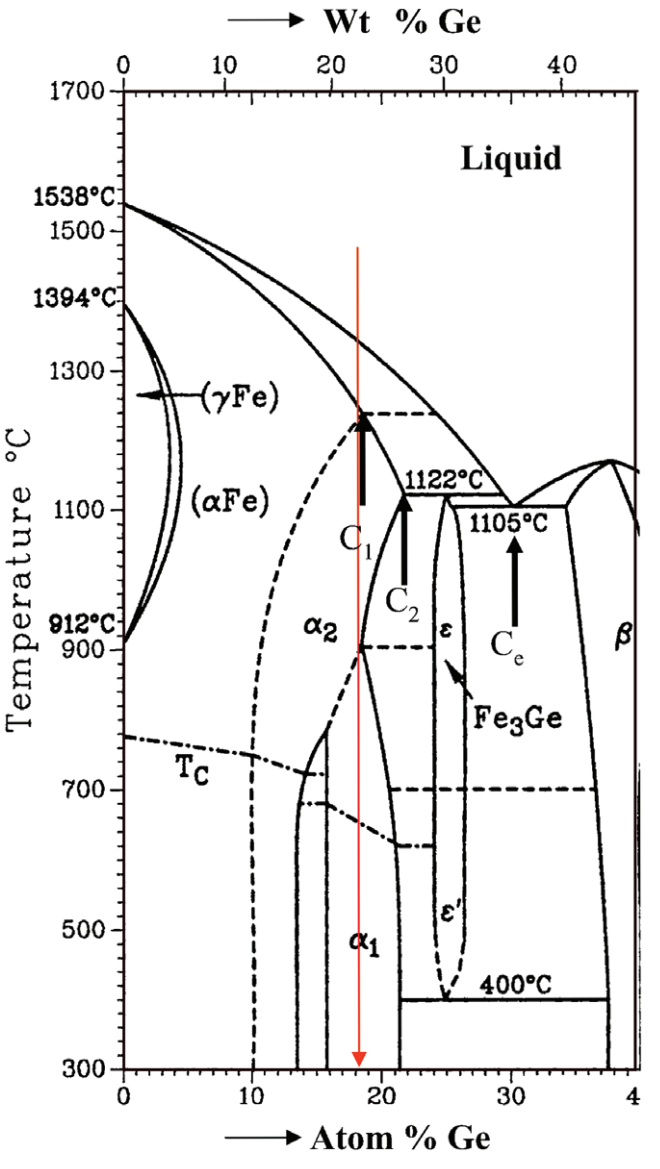

Figure 1. Fe-rich part of the Fe–Ge equilibrium phase diagram [6]. The composition of the chosen alloy is shown by the red arrow.

to the sample. The temperature of the sample was monitored using a two-colour pyrometer with an accuracy of ±5 K and measurement frequency of 100 Hz. Solidification was triggered at the bottom of the droplet using a needle of 99.99% Fe at a desired temperature or level of undercooling. The trigger needle was also part of a capacitance proximity sensor (CPS) that produced a distinct voltage signal coinciding with the triggering event. The end of the solidification was detected by a

photodiode placed on top of the chamber. The time-resolved voltage signals from the capacitance proximity sensor (CPS) and photodiode, both of accuracy better than 10 μs, were measured with a 400-MHz digital oscilloscope. The time difference between the two signals gives the total solidification time. Height of the sample gives the distance travelled by the solid/liquid front in the course of solidification. Complete details of the growth-rate measurement setup are available in [9].

As-cast samples, as well as samples solidified at different undercoolings, were sectioned for further characterization using X-ray diffraction (XRD, JEOL JDX 830) using Fe-Kα radiation ($\lambda = 0.1937$ nm), optical microscopy (OM, Olympus, Tokyo, Japan), field emission scanning electron microscopy (SEM; FEI SIRION) equipped with energy dispersive X-ray analysis (EDX) and electron back-scattered diffraction (EBSD) and transmission electron microscopy (TEM, JEOL 2000FXII). Sectioning of the samples was performed so that the cutting plane was parallel to the plane containing the triggering point. Therefore, the observation plane is always parallel to the heat flow direction. Samples were etched using a mixture of acids (HCl/HNO_3/glacial CH_3COOH, 2:3:1, v/v) to reveal the internal microstructure. Electron back-scattered diffraction (EBSD) analysis was performed on flat electro-polished sections of the undercooled samples with the microscope operating at 25 kV. A solution of 5 vol% perchloric acid in ethyl alcohol was used as the electro-polishing agent. The OIM Data Collection software (OIM is a trademark of EDAX) was used for analysing the data. An orthotropic symmetry was used for the undercooled samples and micro-hardness measurements are done using a Shimadzu hardness tester with a 100-g applied load.

3. Results and discussion

3.1. *Dendritic growth*

The solidification velocity of dendrites as a function of undercooling, derived from the recalescence events of this alloy, is shown in figure 2. The undercooling is given by the difference between the liquidus and nucleation temperatures of the alloy. The error in solidification velocity measurement is estimated to be ~10% at all undercoolings. All data points were evaluated from experiments where the solidification is externally triggered at pre-determined nucleation temperatures. Measurements have been made up to an undercooling level of 210 K. The growth rate is sluggish up to an undercooling of 120 K and then increases rapidly to several m/s at higher undercooling.

The experimentally measured growth rates are compared with the calculated dendrite tip velocity versus undercooling curve according to the Boettinger, Corriel and Trivedi model (BCT model) [10], which is a modification of the work of Lipton *et al.* [11].

The bulk undercooling, ΔT, the difference between the liquidus and the nucleation temperature is the sum of four individual contributions:

$$\Delta T = \Delta T_T + \Delta T_S + \Delta T_R + \Delta T_K \quad (1)$$

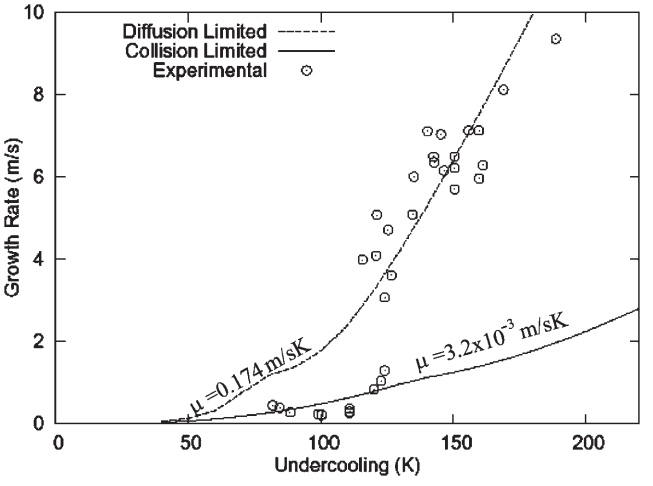

Figure 2. Growth behaviour of Fe–18 at% Ge sample in undercooling experiments. The experimental data points are fitted with different dendrite growth models.

The different terms denote thermal undercooling, ΔT_T, curvature undercooling, ΔT_R, constitutional or solutal undercooling, ΔT_S and the kinetic undercooling, ΔT_K.

Thermal undercooling can be expressed as $\Delta T_T = T_Q Iv(Pe_T)$ where T_Q denotes hypercooling ($\Delta H/C_P^l$), $Iv(Pe_T)$ is the Ivantsov function of thermal Péclet number ($Pe_T = Vr/2D_T$), V the crystal growth velocity, r is the dendrite tip radius and D_T is thermal diffusivity. The Ivanstov function is given by $Iv(Pe_T) = Pe_T \exp(Pe_T) E_1(Pe_T)$ with $E_1(Pe_T)$ as the first exponential integral function.

The solutal undercooling is given by:

$$\Delta T_S = mc_0 \left(\frac{1}{1-(1-k)Iv(Pe_C)} - 1 \right) \tag{2}$$

where m is the velocity-dependent liquidus slope, c_0 the composition of the melt, k_e the equilibrium partition coefficient, $Pe_c = rV/2D_L$ the solutal Péclet number and D_L solute diffusivity. The velocity-dependent liquidus slope is given by $m = m_0[1+(k_e - k + k\ln(k/k_e))/(1-k_e)]$, whereas the velocity-dependent partition coefficient is given by $k = (k_e + V/V_D)/(1 + V/V_D)$, where V_D is the interface diffusive velocity [12]. ΔT_R is given by $2T_M\Gamma/r$, T_M being the liquidus temperature and Γ is the Gibbs–Thomson coefficient. The kinetic undercooling is given by $\Delta T_K = V/\mu$, where the kinetic coefficient μ is given by:

$$\mu = \frac{LV_0}{RT_M^2} \tag{3}$$

L is the heat of fusion and V_0 is a kinetic parameter. It can either be V_s, velocity of sound for collision-limited growth or V_D, diffusive speed for diffusion-limited growth [13]. R is known as the universal gas constant.

Table 1. Values of the thermo-physical parameters used in calculations.

Symbol	Parameter	Unit	Value
T_L	Liquidus temperature	K	1625 K
T_Q	Supercooling	K	456.86
D_T	Thermal diffusivity	m^2/s	1.76×10^{-5}
D_l	Solute diffusivity	m^2/s	5.0×10^{-9}
Γ	Gibbs–Thomson coefficient	Km	2.93×10^{-7}
V_s	Velocity of sound	m/s	200
V_d	Interface diffusive velocity	m/s	5
C_0	Composition of alloy	at%	18
k_e	Equilibrium partition coefficient	no unit	0.78856
m_0	Equilibrium liquidus slope	K/at%	−14.98
L	Heat of fusion	J/mol	19090
C_P	Specific heat of liquid	J/mol/K	41.78
$\mu(=RT_M^2/L)$	Kinetic coefficient	K	1150
σ_0	Solid/liquid interfacial energy	J/m^2	0.348
n	R_{trunk}/R_{tip}	–	20
ε_c	Anisotropy of surface tension of solid-liquid interface	–	1.8×10^{-2}

The BCT theory takes the unconstrained growth of a dendrite into an undercooled alloy melts. From microscopic solvability theory, an independent expression for dendritic tip radius can be obtained [14]. Therefore, the dendrite tip radius r is given by:

$$Vr^2 = \frac{2T_M\Gamma}{\sigma^*\left\{\frac{(T_Q\xi_T}{2D_T)} + \frac{[(2mc_0(k-1))}{D[1-(1-k)Iv(Pe_C)]}\xi_c\right\}} \tag{4}$$

σ^* denotes a stability constant which can be approximated by $\sigma^* = \sigma_0\varepsilon_c^{7/4}$, where σ_0 is a constant and ε_c is the strength of anisotropy of surface tension at the solid–liquid interface. The expressions for stability functions, ξ_t and ξ_c have been described elsewhere [1].

The equations (1) and (4) are solved numerically to determine the unique dendritic tip radius as a function of velocity at different levels of undercooling. The parameters used for the numerical calculation are given in table 1. In the case of non-availability of data, the estimated values from corresponding parameters of the pure components are used in the calculation [15]. Such an approximation is reasonable as the phase for which the growth rate is analyzed is a solid solution of germanium in iron. Owing to the non-availability of data of ε_c, its value has been taken from the atomistic simulation of Sun *et al.* [16].

Theoretical results are plotted in figure 2. The computed growth curve as a function of undercooling indicates the range of undercooling where a particular growth model is valid. It can be observed that the experimental measurements at a low undercooling regime ($\Delta T < 120$ K) indicate ordered growth, as the low growth rates could only be modelled using a low kinetic coefficient of 3.2×10^{-3} m/(sK) in equation (3), which corresponds to $V_0 = V_d$. At undercooling larger than 120 K, the experimentally measured growth rates lie closer to the models that use

collision-limited growth with a kinetic coefficient of 0.174 m/(sK). Corriell and Turnbull [17] first established the limiting velocity (which corresponds to the maximum value of kinetic coefficient) as the velocity of sound in liquid melt, which is taken as $2000\,\mathrm{ms}^{-1}$. Using the velocity of sound as the limiting velocity, the maximum predicted value of the kinetic coefficient will be 1.74 m/(sK). Therefore, the figure suggests that the actual value of the kinetic coefficient in Fe–18 at% Ge alloy is an order of magnitude less than the maximum predicted value [17]. A deviation from the theoretical values of the kinetic coefficient has also been observed in other systems. Hoyt *et al.* [16, 18] performed atomistic simulations to determine the kinetic coefficient for pure metals, such as Au, Ag, Cu and Ni. These authors reported kinetic coefficient values as low as 0.1 m/sK for pure gold using atomistic computation. In view of the non-availability of kinetic coefficient data for solidification of concentrated alloys in the literature, kinetic coefficient, μ, is used in the present investigation as the only free parameter to fit the experimental data.

It has been observed that the experimental data on growth behaviour of ordered intermetallic compounds and theoretical predictions agree if a low kinetic coefficient value (corresponding to $V_0 = V_D$ in the equation (3)) is used [16–18]. This is reasonable because the formation of ordered intermetallic compounds requires short-range diffusion processes of atoms to particular lattice sites and, thereby, crystal growth cannot be predicted using collision-limited growth applicable for disordered solid solutions and pure metals.

This theoretical analysis is substantiated by transmission electron microscopy (TEM) of the undercooled samples. Figure 3a and b show diffraction patterns obtained from a sample undercooled by 140 K along [001] and $[01\bar{1}]$ zone axes, respectively. The $[01\bar{1}]$ pattern clearly indicates the presence of DO_3-ordering in the sample. The dark-field image taken using B2 superlattice reflection of (200)-type (figure 3c) shows the presence of B2 domains. The presence of large number of anti-phase domains suggests that the bcc phase has nucleated directly from the liquid and has undergone ordering reaction in solid state. The superlattice dark-field image using unique DO_3 reflection of $(11\bar{1})$-type, as shown in the inset of figure 3c, reveals very fine scale DO_3 domains. A similar study on samples undercooled below 120 K does not reveal B2 domains.

An important aspect of the rapid solidification behaviour of this alloy is the formation of B2 at lower levels of undercooling ($\Delta T < 120$ K). This can be attributed to dendrite coring, which is a non-equilibrium phenomenon. Coring leads to microsegregation along the primary trunk as well as in the interdendritic regions. In the present case, coring influences phase formation because the associated compositional change leads to change in the phase field. Figure 4a shows compositional profile along the trunk of a primary dendrite in the sample undercooled by 50 K. The inset shows a back-scattered image of the dendrite. The compositional profile has been obtained along the white line marked on the figure. The compositional measurements indicate that the dendrite starts growing at a composition of 14.2 at%. However, germanium concentration increases to ~29.0 at% at the tip of the dendrite. Comparing these measurements with the phase diagram (figure 1) reveals that the dendrite will enter the B2 phase field very rapidly ($>C_2$). In the phase diagram, C_e is indicated as the eutectic composition, C_2 as maximum solubility of germanium in the α_2 phase and C_1 as the solid composition

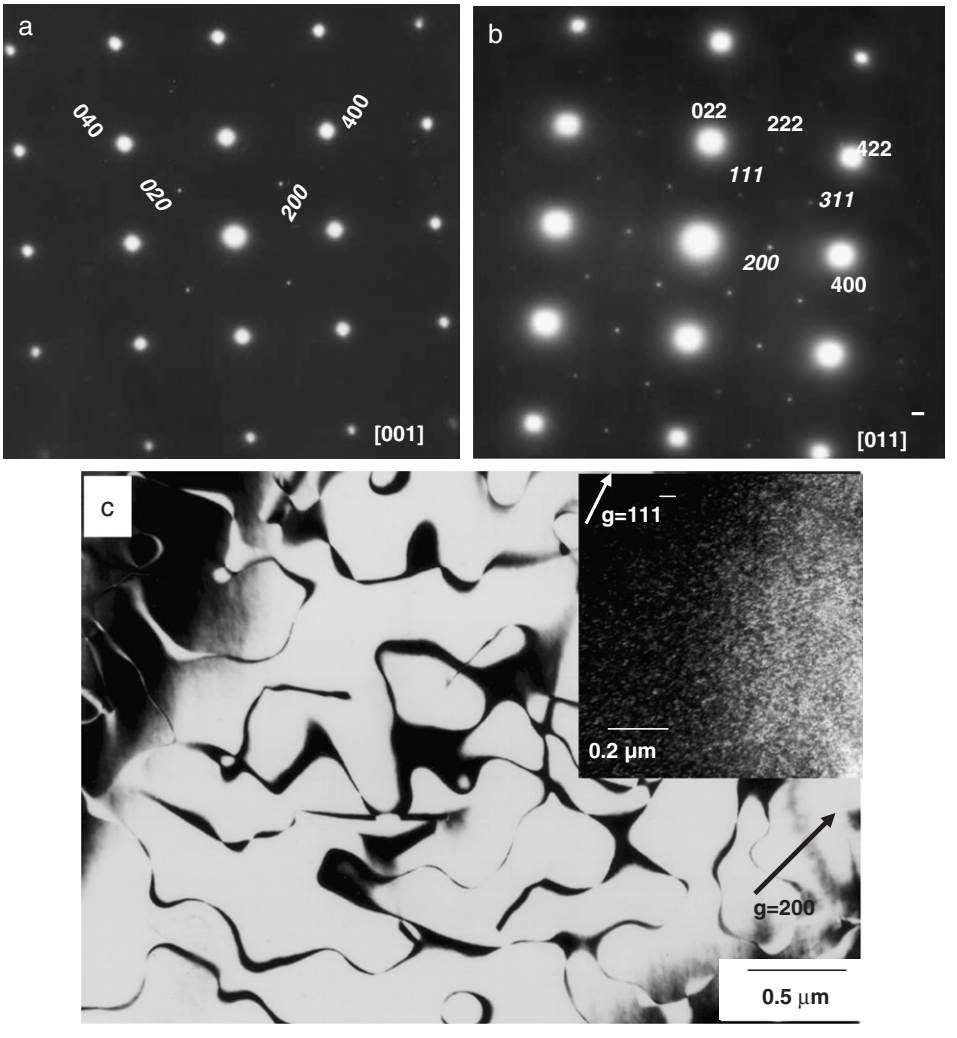

Figure 3. SAD patterns from a sample undercooled by 140 K and quenched along (a) [001] and (b) [01$\bar{1}$] directions, showing the presence of DO_3 ordering and (c) the presence of large numbers of B2 anti-phase domains, with inset showing fine scale DO_3 domains.

denoted by B2 ordering transition intersecting the solides of α phase. Similar measurements (data not shown) across the dendrite trunks also reveal segregation of solute in the interdendritic regions.

The composition of a solidifying dendrite under non-equilibrium conditions can be estimated using Scheil's equation under the condition of no diffusion in solid and complete mixing in liquid. Figure 4b shows a plot of solid composition as a function of the solid fraction. It is clear that part of the dendrite will have a composition more than C_2 (=18.5 at%). Therefore, in case of low undercooled samples (<120 K), bcc dendrites will grow at the beginning. However, coring will shift the composition of

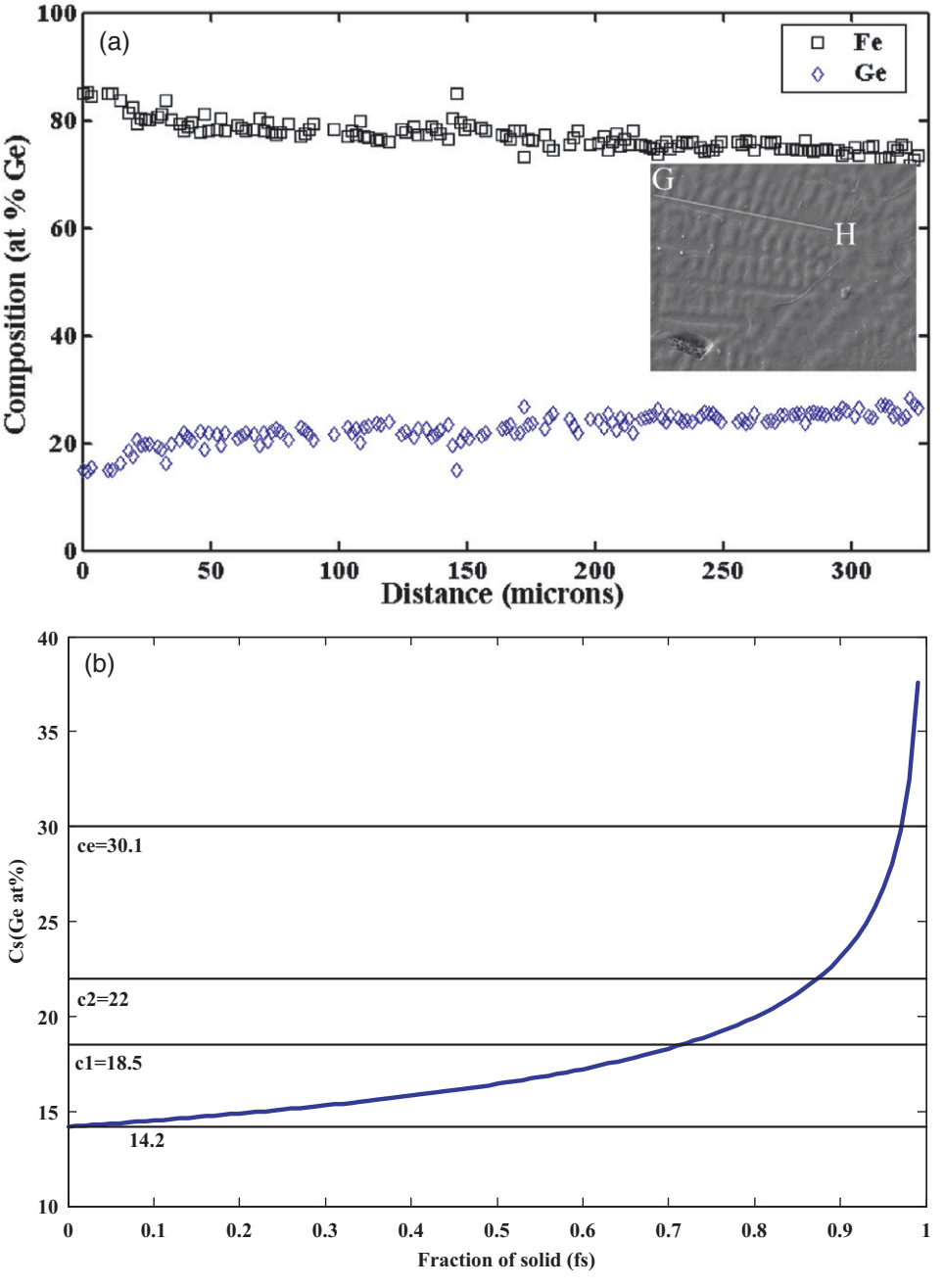

Figure 4. (a) Compostiton profile along the primary trunk of sample undercooled SOK showing solute enrichment and (b) calculated composition profile as a function of fraction of solid using Scheil's equation.

the solidifying dendrite so that the remaining part of the dendrite will be growing as B2 phase. Similar behaviour has been observed previously in the growth of Ni–Al solid solution during laser processing [19]. This is consistent with the experimentally measured growth rate, which suggests that growth of B2 phase is favourable to bcc at low undercooling regime ($\Delta T < 120$ K).

3.2. *Grain microstructure of levitated droplets*

This section details the experimental results on the grain microstructures of alloy droplets solidified at different levels of undercooling. The microstructure of the as-cast sample (data not shown) shows a single-phase microstructure with large grains (grain size: 100–200 μm). Careful etching revealed the dendritic patterns inside these grains. EBSD analysis was performed on electro-polished sections of the undercooled samples and a typical EBSD pattern from droplets undercooled by 130 K is shown in figure 5a. The pattern can be indexed using a B2 unit cell ($a = 0.288$ nm), as shown in figure 5b. The microstructure and EBSD analysis of the undercooled samples to characterize the grains in these samples is presented below.

3.2.1. Low undercooling ($\Delta T \leq 110$ K). Figure 6a shows the optical microstructure of samples undercooled by 50 K. The microstructure shows large grain size with a coarse dendritic segregation pattern. This figure also reveals the formation of an equiaxial dendritic microstructure. Figure 6b shows the optical microstructure of a sample undercooled by 110 K. The dendrite segregation pattern is still clearly visible with the dendritic substructure extending across the grain boundaries. The black dots seen in the microstructures are etch pits. The inset in figure 6b shows the plot of grain misorientation angle versus fraction of grains obtained from EBSD analysis of the sample undercooled by 110 K. Most of the grain boundaries are of the high angle type (grain misorientation angle $>15^\circ$); there are few ($\sim$10%) grains with misorientation angles $<5^\circ$.

3.2.2. Intermediate undercooling ($110\,\text{K} < \Delta T \leq 140$ K). As the undercooling increases, a change in microstructure is observed. Figures 6c and d depict optical micrographs of samples undercooled by 130 and 140 K respectively. Figure 6c shows that grains are aligned along certain directions, whereas this is not the case in samples undercooled by 140 K (figure 6d). The inset in figure 6d reveals the presence of small fragmented dendrites. In both cases, one can observe smaller grains inside the outline of larger grains (see inset 1 of figure 6c). Some of the grains in figure 6d show the presence of very small sub-grains (indicated by a white arrow). Thus, both high- and low-angle grain boundaries are evident in the micrograph (as evident from inset 2 of figure 6c). This appearance is not uniform across all the grains. The shape of the grains and curved nature of the grain boundaries (some of them are marked by black arrows on figure 6d) suggests appreciable grain growth. EBSD analysis of the sample undercooled by 130K is shown as inset 2 of figure 6c. Approximately 40% of the grain boundaries are of the low-angle type (misorientation angle $<15^\circ$).

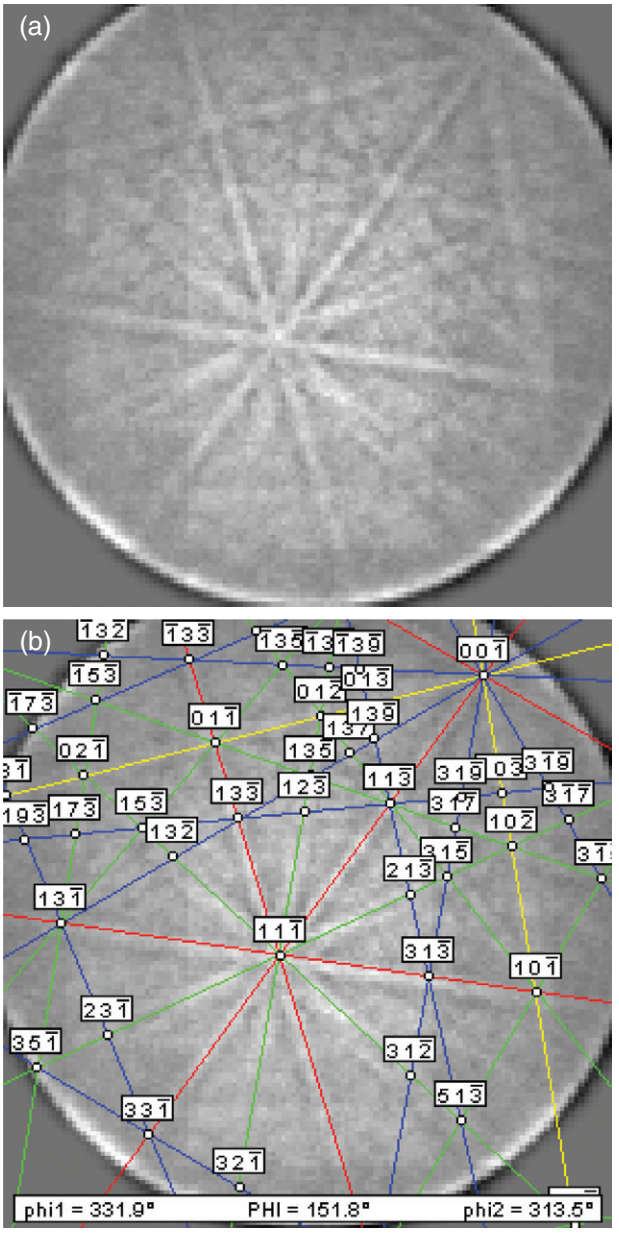

Figure 5. EBDS pattern obtained from (a) an undercooled sample and (b) pattern indexed using a B2 unit cell ($a = 0.2288$ nm).

3.2.3. High undercooling ($\Delta T \geq 160$ K). Figure 6e and f show optical micrographs of samples undercooled by 190 and 240 K. The dendrite segregation pattern could not be detected in either case. The grain size is much finer than the samples solidified at

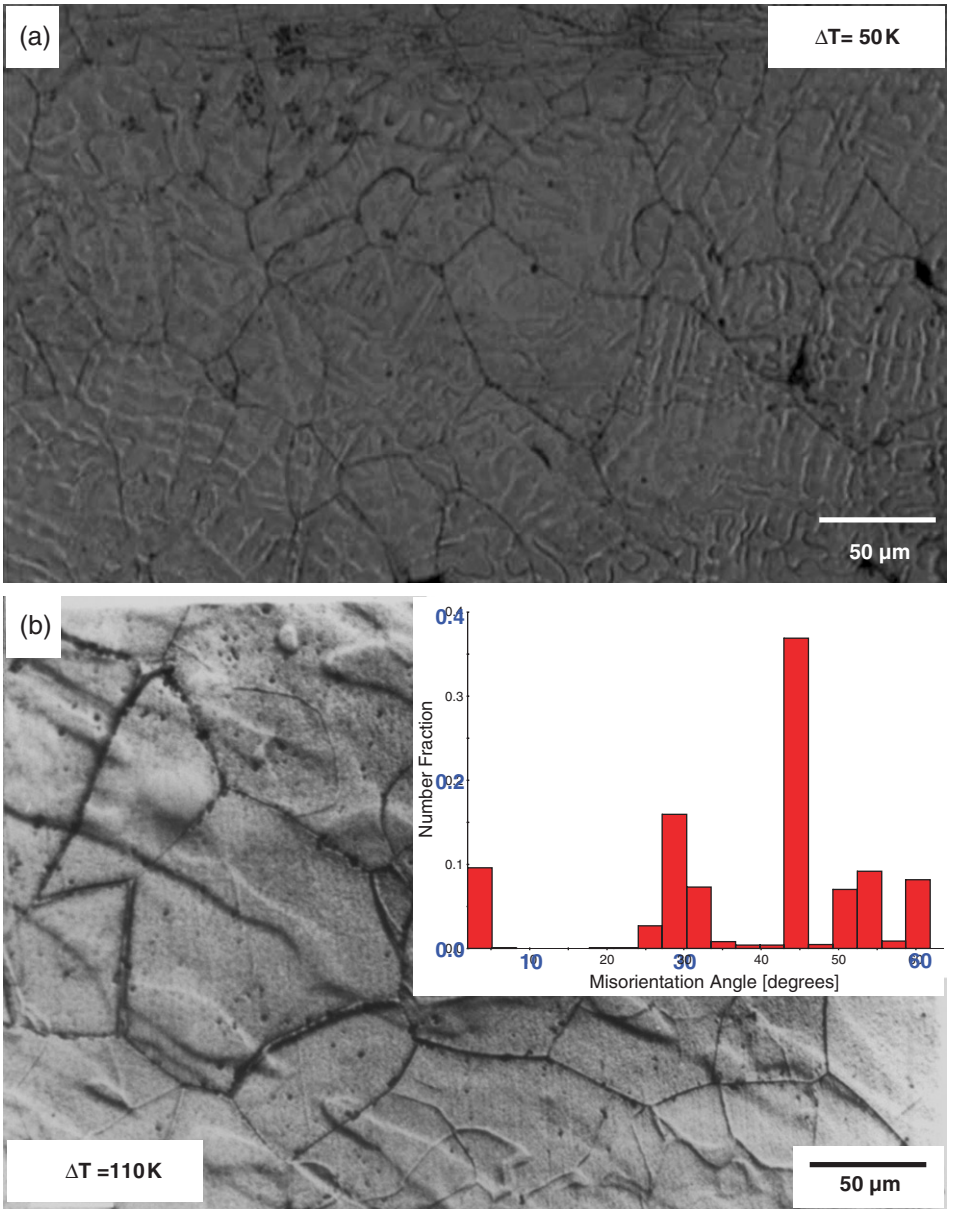

Figure 6. Optical micrographs showing the microstructure of samples at different levels of undercooling: (a) $\Delta T = 50\,\mathrm{K}$, (b) $\Delta T = 110\,\mathrm{K}$, with inset showing grain boundary characteristics, (c) $\Delta T = 130\,\mathrm{K}$, with inset 1 showing a higher magnification micrograph of a large number of small grains inside a well-defined large grain and inset 2 showing grain boundary characteristics, (d) $\Delta T = 140\,\mathrm{K}$, with inset showing a higher magnification micrograph of dendrite fragments within the grains, (e) $\Delta T = 190\,\mathrm{K}$, with inset showing grain boundary characteristics and (f) $\Delta T = 240\,\mathrm{K}$.

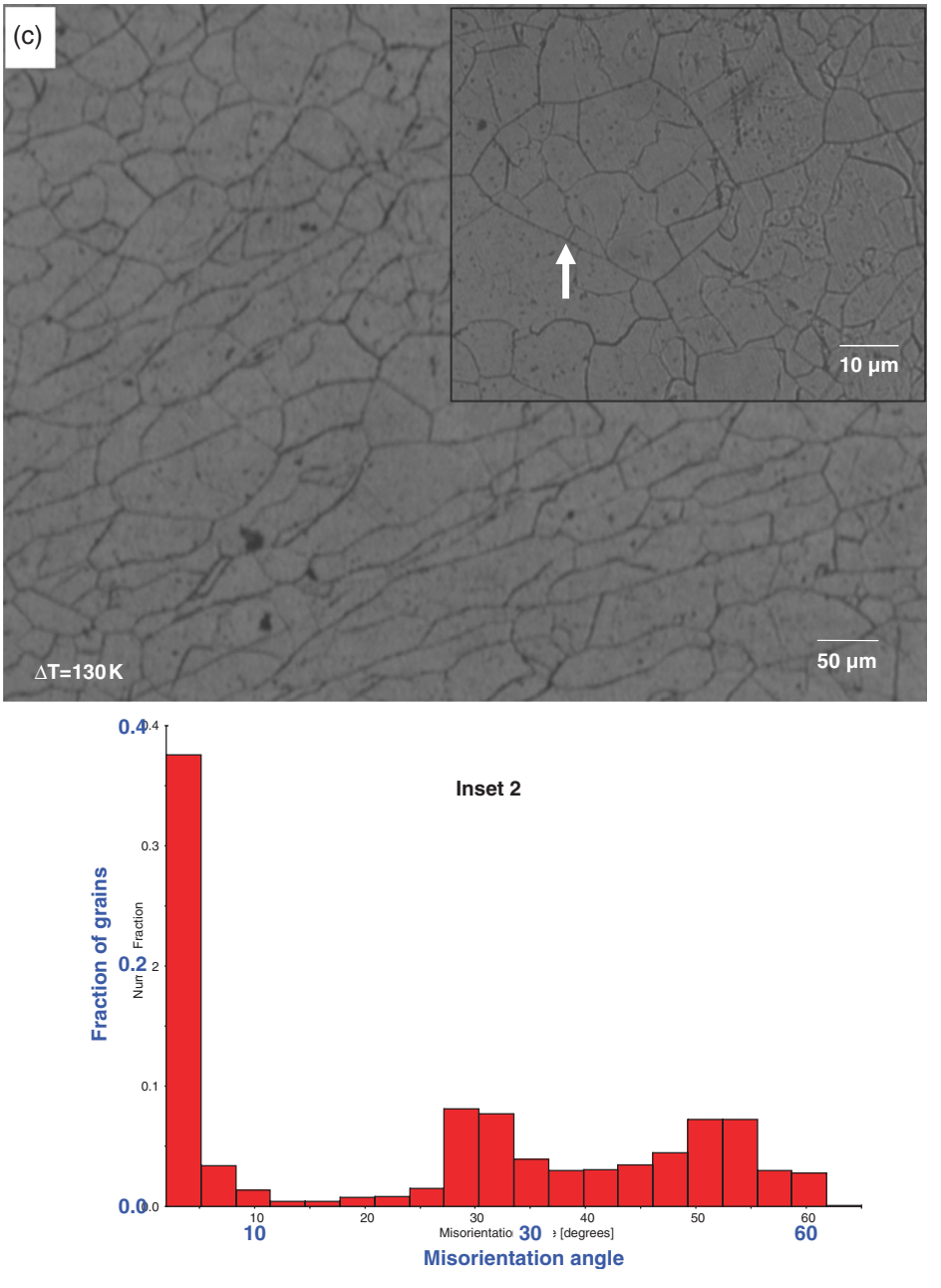

Figure 6. Continued.

intermediate undercooling regimes. The presence of finer grains or sub-grains is evident in figure 6e and this effect is uniform across the all grains. The inset of figure 6e represents grain orientation versus fraction of grains obtained from EBSD analysis. The presence of a large fraction (40%) of small-angle grain boundaries

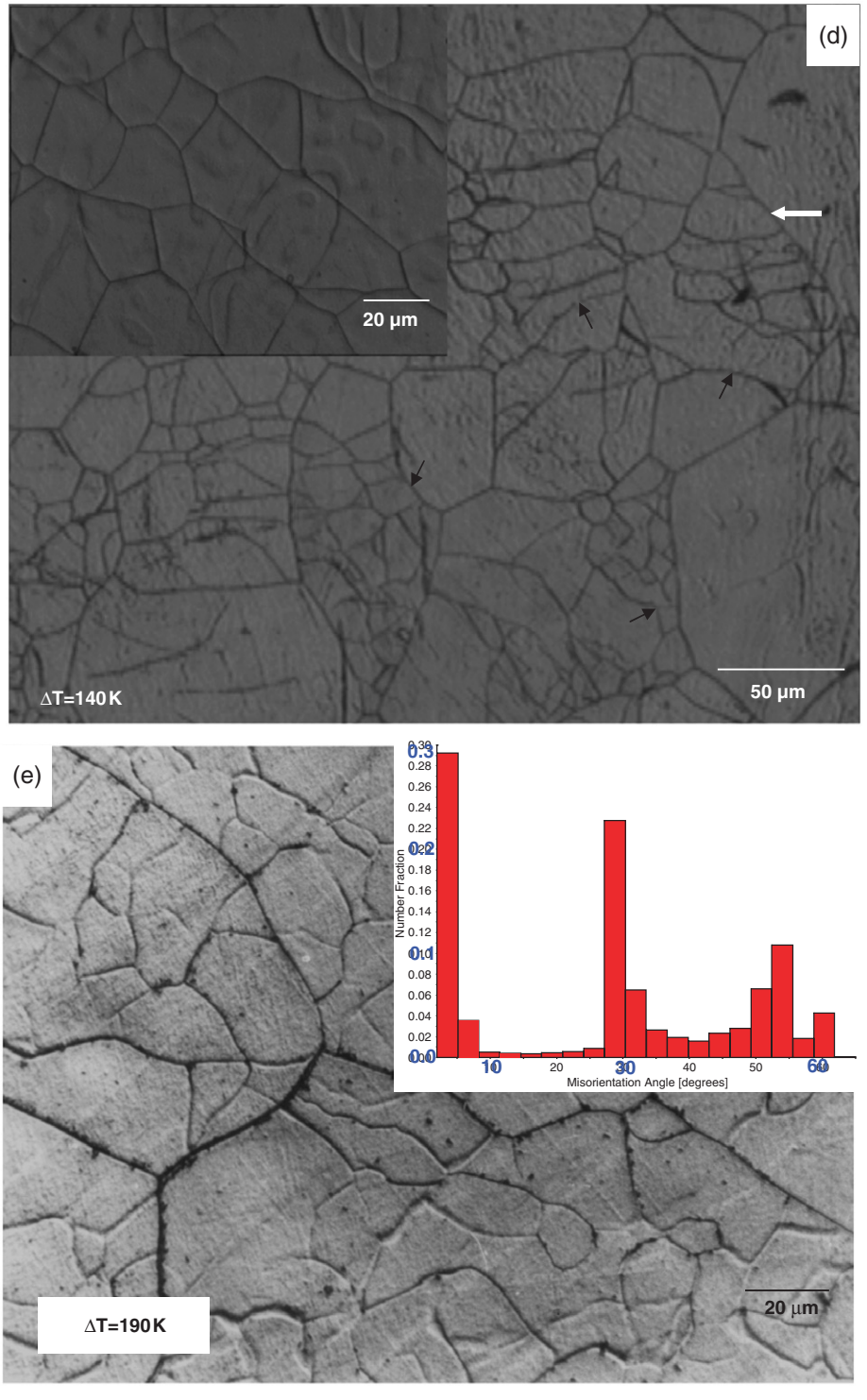

Figure 6. Continued.

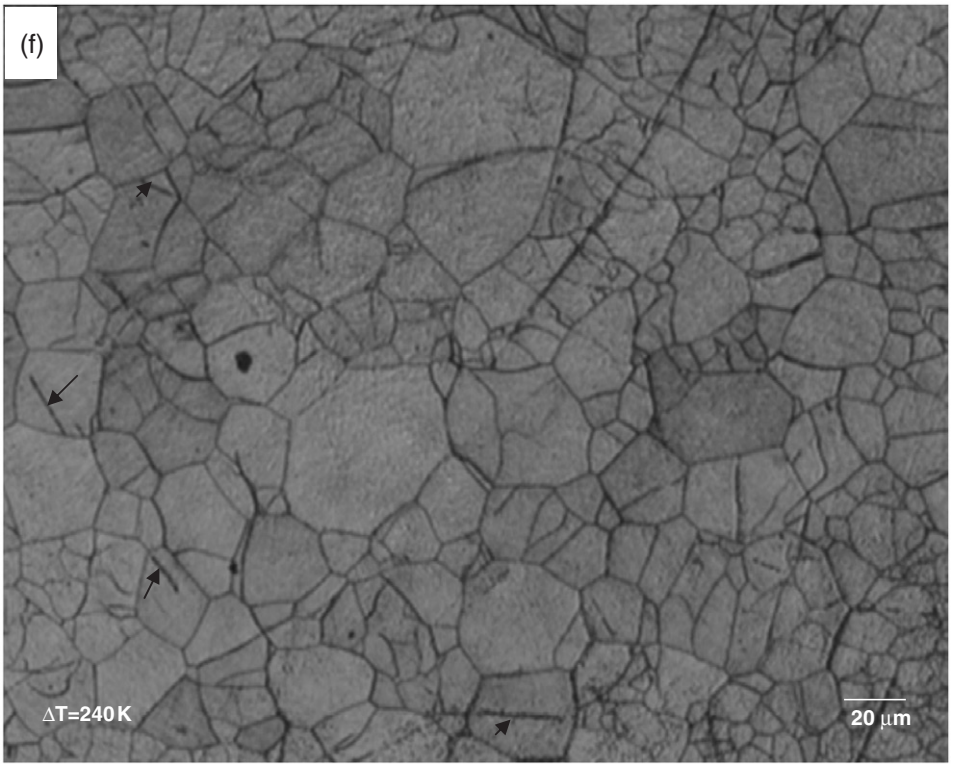

Figure 6. Continued.

(<15° of misorientation angle) has been observed for the sample undercooled by 190 K. Grain size is even finer, but not uniform, in the case of samples undercooled by 240 K (figure 6f). This microstructure also shows the occasional presence of twins. Some of the twins are marked on the micrograph by black arrows.

Figure 7a shows the average grain size of the samples undercooled at different levels. Note that grain size is large (>100 μm) up to an undercooling of 100 K but there is a sudden drop in grain size for the sample undercooled by 130 K. Thus, grain size decreases by an order of magnitude. At higher levels of undercooling, the grain size does not change significantly. Microhardness measurements were made on samples solidified at various levels of undercooling, as shown in figure 7b. Microhardness increases to a maximum value of hardness of 1200 kgf/mm^2 at an undercooling of 120 K and then decreases with a further increase in undercooling to 900 kgf/mm^2 at $\Delta T = 160$ K.

3.2.4. Mechanisms of grain refinement. The results presented above suggest a significant decrease in grain size with undercooling. There are a number of theories in the literature for elucidating the mechanisms responsible for intrinsic grain

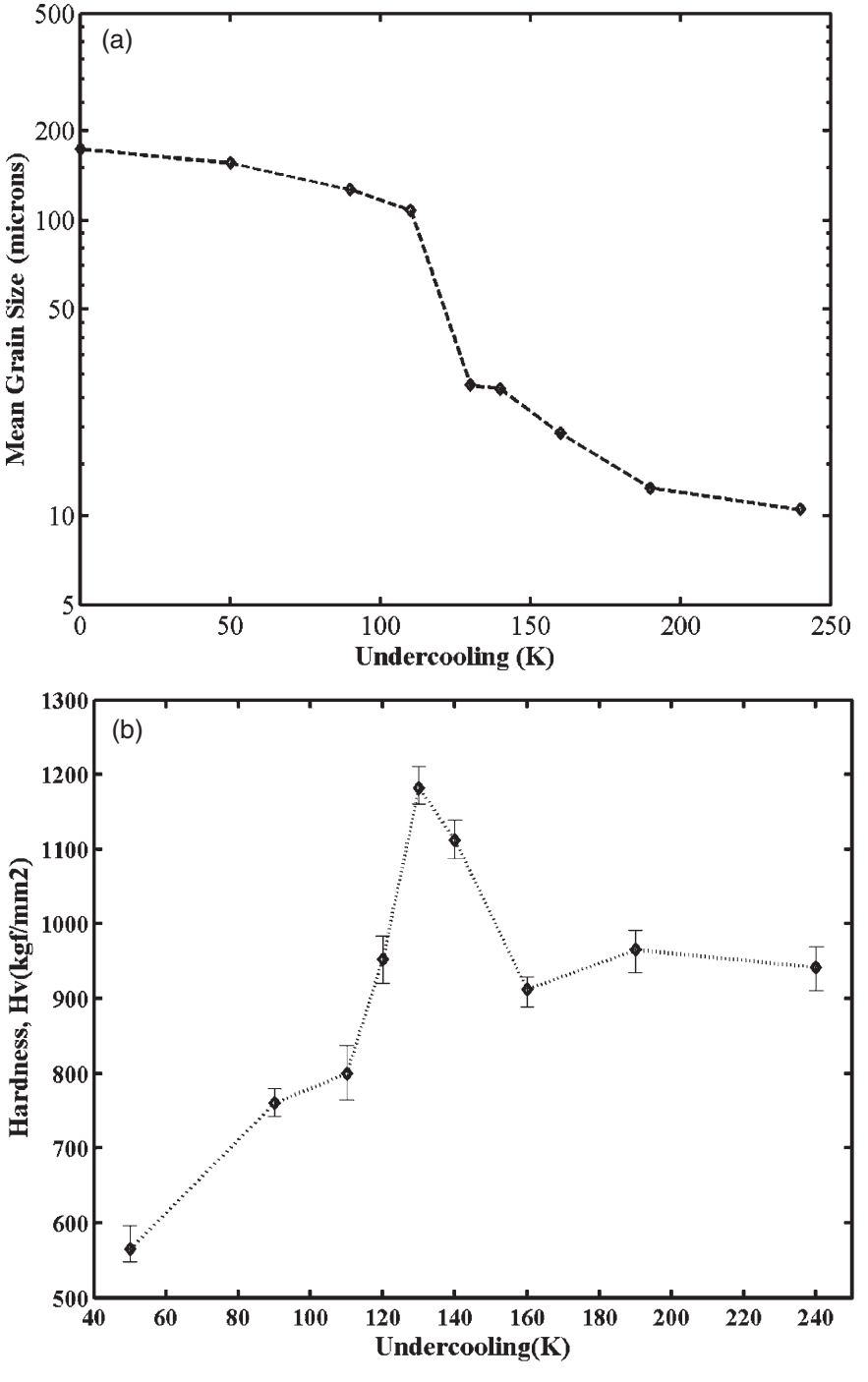

Figure 7. (a) Grain size versus levels of undercooling and (b) microhardness versus undercooling plots.

refinement during solidification from undercooled melt. They can be categorized as follows:

(a) Copious nucleation due to pressure pulse associated with solidification [20]
(b) Dendrite remelting and fragmentation [21]
(c) Recrystallization either during or immediately following solidification [22]

If copious nucleation were responsible for grain refinement in the present case, then the grain structure should be equiaxial regardless of the time taken to complete solidification. This does not appear to be the case from the microstructural studies of highly undercooled samples (figures 6e and f). Therefore, the first case can be ruled out.

A number of studies suggest that dendrite fragmentation is the prominent mechanism of spontaneous grain refinement during solidification from the undercooled melt [4, 21, 23, 24]. However, other experimental studies also indicate recovery and recrystallization after recalescence as being responsible for spontaneous grain refinement [5, 22, 25, 26] in the undercooled melt. The processes of dendrite fragmentation and recrystallization will differ depending on materials properties. The validity of the dendrite fragmentation model will be discussed first.

Karma [21, 23] developed a model for dendrite fragmentation based on the morphological instability of a solid cylinder embedded in its melt leading to fragmentation of the cylinder into spheres. The driving force for this process is the reduction of the solid–liquid interfacial area. There are two characteristic time scales which enter into the model: the dendrite break-up (t_{bu}) time, corresponding to recalescence time, and the thermal plateau time, corresponding to the post-recalescence solidification period (t_{pl}). According to this model, grain refinement can be expected when the thermal plateau time for solidification (t_{pl}) exceeds the time required for break-up of dendrites (t_{bu}). Therefore, the transition at critical level of undercooling (ΔT^*) from the coarse dendrite microstructure to the equiaxial microstructure is possible when:

$$t_{bu}(\Delta T^*) = t_{pl}(\Delta T^*) \tag{5}$$

The plateau time, t_{pl} is exclusively controlled by the heat transfer from the sample to the environment. Therefore, it is an experimentally controlled parameter, which can be measured. The levels of undercooling, ΔT and corresponding plateau time t_{pl}, are directly inferred from the temperature–time profile.

Karma [21] calculated the break-up time (t_{bu}) for a binary alloy as follows:

$$t_{bu}(\Delta T) = \frac{3R_{trunk}(\Delta T)^3}{2D_T d_0}\left[1 - \frac{m_0 C_0(1-k_e)D_T}{(\Delta H_f/C_P^l)D_l}\right] \tag{6}$$

where R_{trunk} is the radius of the dendrite trunk, D_T is thermal diffusivity, D_l is solute diffusivity in liquid, m_0 is the equilibrium liquidus slope, k_e is the equilibrium partition coefficient, ΔH_f is heat of fusion, C_P^l the specific heat of liquid at the solidification temperature, $d_0 = \Gamma C_{Pl}/\Delta H_f$ is the capillarity length, Γ is the Gibbs-Thomson coefficient and c_0 is the solute concentration in the binary alloy.

To calculate t_{bu} as a function of ΔT, the variation in R_{trunk} with ΔT must be known. There are no satisfactory dendrite growth models available in the literature

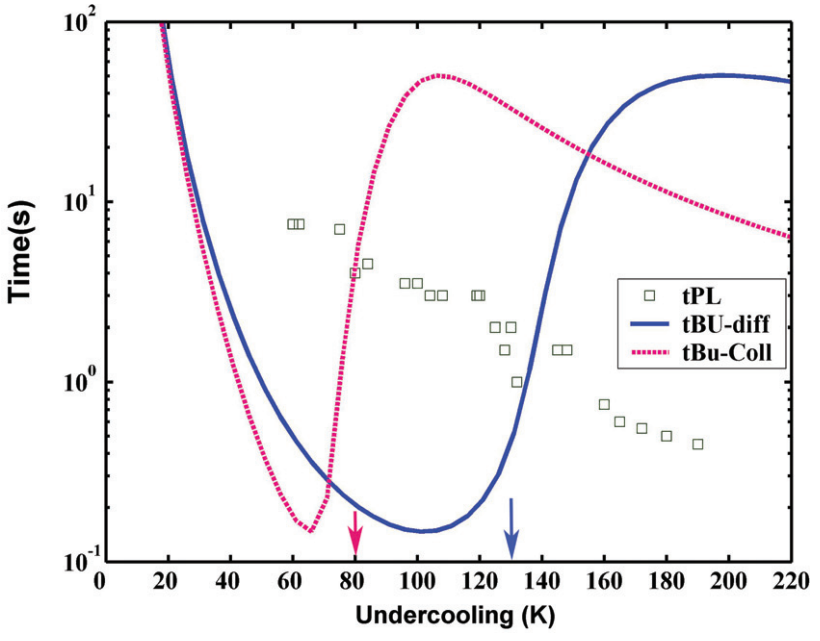

Figure 8. Calculated dendrite break-up time (t_{bu}) versus undercooling curve (dotted line) and measured plateau durations (t_{pl}) versus undercooling (open square). The arrow shows the transition temperature (or undercooling). The dotted line is obtained using the Karma model [21].

that predict the trunk radius as a function of undercooling. However, most of the dendrite models predict the radius of curvature, R_{tip}, at the tip by assuming the tip to be a paraboloid of revolution [27]. Therefore, the trunk radius, R_{trunk}, has to be approximated from the tip radius, R_{tip}. One way of doing this is to take $R_{trunk} = nR_{tip}$, where n is a constant and R_{tip} can be obtained as a function of levels of undercooling using microscopic solvability criteria [14]. A comparison of the computed values of the tip radius (R_{tip}) with the measured trunk radius (R_{trunk}) from studies on transparent organics [28], yields $n \approx 20$ and n is roughly independent of undercooling. Thermophysical data used for the calculation of t_{bu} is given in table 1.

Using such a relationship between R_{tip} with undercooling (ΔT), the calculated break-up time (t_{bu}) [21, 23] is plotted against undercooling, as shown in figure 8 for both diffusion- and collision-controlled growth models. The break-up time sharply decreases with undercooling; passing through a minimum, then rising again steeply and, finally, going through a maximum before falling again. The plateau time (t_{pl}), inferred from temperature–time profile, is also plotted on the same figure as open squares. Note that the point showing the plateau time intersects the break-up time at a critical level of undercooling. According to the Karma model, the intersection points satisfy equation (5). Transition undercooling, computed using the collision-controlled growth model ($\Delta T_*^{coll} = 80$ K) is found to be lower than that ($\Delta T_*^{diff} = 130$ K), predicted by the diffusion-controlled growth model. However, experimentally observed growth velocity data can be fitted with the

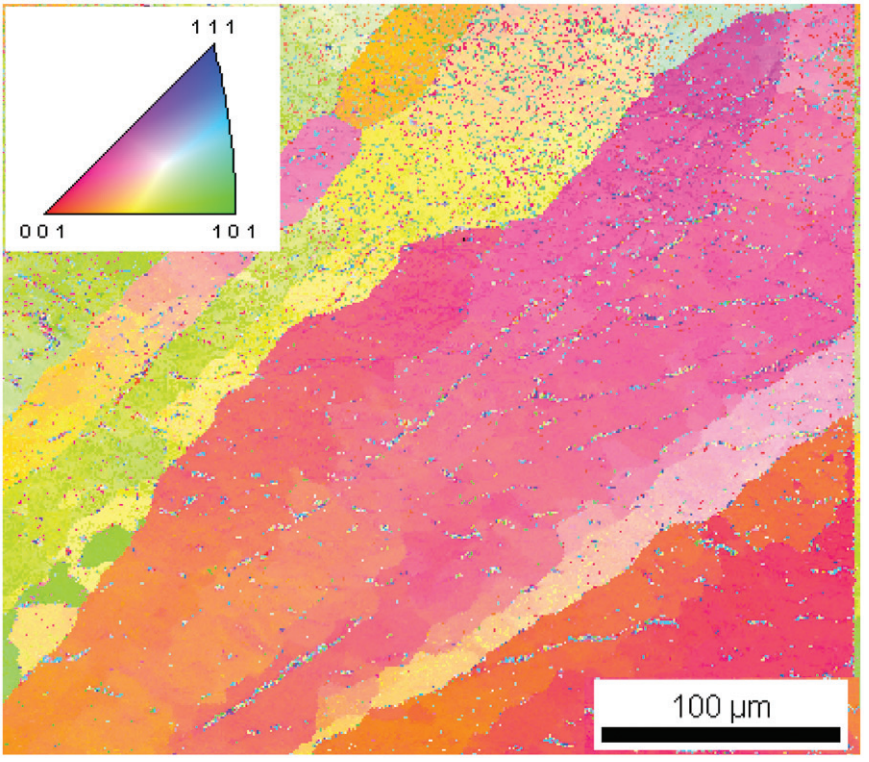

Figure 9. EBSD grain map of the sample undercooled by 130 K. (For colour vesion, see online).

diffusion-controlled growth model at lower undercooling regimes ($\Delta T < 120$ K). Both the collision- and diffusion-limited growth assumptions confirm that Karma's model predicts grain refinement at undercoolings close to the experimentally observed values. Thus, within the scope of assumptions made to estimate the necessary parameters, a sudden decrease in grain size can be adequately rationalized by the Karma model.

However, EBSD analysis indicates a large number of low-angle grain boundaries in the intermediate and high undercooled samples. In the dendrite fragmentation model, each fragmented dendrite in the melt determines the crystal orientation of that grain. Since convective flow is expected to randomize the orientation of these fragments, one should not expect a large peak at low angles for grain orientation. The low-angle boundary clearly indicates a recovery process and the presence of the growth twin indicates a recrystallization process. The sub-grain boundaries, as shown in the inset of figure 6c, cannot be explained by the dendritic fragmentation model and such features are abundant in the high undercooled samples. Figure 9 shows an EBSD map of the sample undercooled by 130 K. The colour map depicts the grains with orientation varying by 2°. Therefore, the colour variation will indicate the presence of low-angle grain boundaries. Note the presence of a large number of low-angle grain boundaries within large grains. In fact, it has been found

that the fraction of low-angle grain boundaries (misorientation angle $<15^{\circ}$) is about 0.5. The presence of such large fraction of low-angle grain boundaries is a clear indication of a process of recovery which the sample has undergone in the solid state after recalescence. Currently, it is not possible to calculate stresses in the growing crystals due to lack of mechanical property data at high temperature for the Fe–Ge alloy and the absence of a model which can estimate the source of stresses due to fluid flow and impingement of dendrites. However, experimental data clearly indicate a significant increase in hardness of samples undercooled in the range 120–140 K, which can only be explained by the presence of residual stresses. Thus, we conclude that recovery and probably recrystallization in the solid state plays a significant role in the evolution of the fine grains in undercooled Fe–Ge samples.

5. Conclusions

The present investigation shows that

(1) At low undercooling (<120 K), the primary phase is ordered B2, while at higher undercoolings (>120 K), it is the bcc phase. Experimental data on growth rates indicate disorder trapping. The measured growth rates are consistent with the current models of dendrite growth in undercooled liquid, taking into account the structural change of the growing solid.
(2) There is a spontaneous grain refinement in the samples as undercooling increases. Microstructural investigations indicate that the processes of recovery and recrystallization play a role in grain refinement, although dendrite fragmentation leading to grain refinement cannot be excluded.

Acknowledgements

One of the authors (GP) would like to thank the AvH Foundation for support through a research fellowship. This research was supported by a project between Department of Science and Technology (DST), Government of India and Bundesministerium für Bildung und Forschung (BMBF), Germany. The authors would like to thank Dr Peter Galenko for making his code available for computation of dendrite growth velocity and dendrite tip radius. The manuscript preparation was completed during K.B.'s stay at Tohoku University. K.B. would like to thank the Japan Society for Promotion of Sciences (JSPS) for a research followship.

References

[1] D.M. Herlach, Mater. Sci. Eng. Rep. R **12** 177 (1994).
[2] R.W. Cahn, P.A. Simmers and E.L. Hall, Acta Metall. **36** 2763 (1982).
[3] J.A. Est, J.T. Manos and M.J. Aziz, Mater. Res. Soc. Symp. Proc. **364** 41 (1994).

[4] A.F. Norman, K. Eckler, A. Zamdon, *et al*., Acta Mater. **46** 3355 (1988).
[5] S.E. Battersby, R.F. Cochrane and A.M. Mullis, J. Mater. Sci. **35** 1365 (2000).
[6] T.B. Massalski, *Binary Alloy Phase Diagrams*, 2nd ed. (ASM International, Materials Park, OH, USA, 1999), p. 1704.
[7] K. Raviprasad, S. Ranganathan and K. Chattopadhyay, Scripta Metall. Mater. **26** 467 (1992).
[8] E. Schleip, R. Willnecker, D.M. Herlach, *et al*., Mater. Sci. Eng. **98** 39 (1988).
[9] K. Eckler, M. Kratz and I. Egry, Rev. Sci. Instrum. **64** 2639 (1993).
[10] W.J. Boettinger, S.R. Corriell and R. Trivedi, in *Proceedings of the 4th Conference on Rapid Solidification Processing: Principles and Technologies*, edited by R. Mehrabian and P.A. Parrish. (Claitors, Baton Rouge, LA, 1987), p. 13.
[11] J. Lipton, W. Kurz and R. Trivedi, Acta Metall. **35** 957 (1987).
[12] M.J. Aziz, J. Appl. Phys. **53** 1158 (1982).
[13] M.J. Aziz and W.J. Boettinger, Acta Metall. Mater. **42** 527 (1994).
[14] D.M. Herlach and P.K. Galenko, Mater. Sci. Eng. A **449/451** 34 (2007).
[15] E.A. Brandes, *Smithell's Metals Reference Book*, 6th ed. (Butterworth, London, 1983).
[16] D.Y. Sun, M. Asta and J.J. Hoyt, Phys. Rev. B **69** 024108 (2004).
[17] S.R. Corriel and D. Turnbull, Acta Metall. **30** 2135 (1982).
[18] J.J. Hoyt and M. Asta, Phys. Rev. B **65** 214106 (2002).
[19] S. Bysakh, S. Mitra, G. Phanikumar, *et al*., Metall. Mater. Trans. A **34** 2621 (2003).
[20] G. Horvay, Int. J. Heat Mass Transfer **8** 192 (1965).
[21] A. Karma, Int. J. Non-Equilib. Process. **11** 201 (1998).
[22] K.I. Dragneski, R.F. Cochrane and A.M. Mullis, Mater. Sci. Eng. A **375/377,** 479 (2004).
[23] M. Schwarz, A. Karma, K. Eckler, *et al*., Phys. Rev. Lett. **73** 1380 (1994).
[24] K. Eckler, A.F. Norman, F. Gärtner, *et al*., J. Cryst. Growth **173** 528 (1997).
[25] G.L.F. Powell and L.M. Hogan, Trans. Metall. Soc. AIME **242** 2133 (1968).
[26] L. Feng and Y. Geneang, J. Cryst. Growth **231** 295 (2001).
[27] G.P. Ivanstov, Dokl. Akad. Nauk SSSR **58** 567 (1947).
[28] U. Bisang and J. Bilgram, Phys. Rev. E **54** 5302 (1996).